

1 **Global prediction of soil saturated hydraulic conductivity using**
2 **random forest in a Covariate-based Geo Transfer Functions**
3 **(CoGTF) framework**

4 **Surya Gupta¹, Tomislav Hengl^{2,3}, Peter Lehmann¹, Sara Bonetti^{1,4}, Andreas Papritz¹, Dani**
5 **Or^{1,5}**

6 ¹Soil and Terrestrial Environmental Physics, Department of Environmental Systems Science, ETH Zürich, Zürich,
7 Switzerland

8 ²Envirometrix Ltd., Wageningen, the Netherlands

9 ³OpenGeoHub, Wageningen, the Netherlands

10 ⁴Bartlett School of Environment, Energy and Resources, University College London, London, UK

11 ⁵Division of Hydrologic Sciences, Desert Research Institute, Reno, NV, USA

12 **Key Points:**

- 13 • Climate, vegetation and terrain affect spatial patterns of saturated hydraulic conductiv-
14 ity (Ksat)
- 15 • The effect of these covariates on Ksat is quantified using remote sensing data and machine
16 learning
- 17 • We introduce geotransfer functions to improve Ksat predictions based on pedotransfer func-
18 tions

Corresponding author: Surya Gupta, surya.gupta@usys.ethz.ch

19 Abstract

20 The saturated hydraulic conductivity (Ksat) is a key soil hydraulic parameter for representing in-
21 filtration and drainage in Earth system and land surface models. For large scale applications, Ksat
22 is often estimated from pedotransfer functions (PTFs) based on easy-to-measure soil properties
23 like soil texture and bulk density. The reliance of PTFs on data from uniform arable lands and
24 omission of soil structure limits the applicability of texture-based predictions of Ksat in vege-
25 tated lands. A method to harness technological advances in machine learning and availability of
26 remotely sensed surrogate information to derive a new global Ksat map at 1-km resolution us-
27 ing terrain, climate, vegetation, and soil covariates is proposed. For model training and testing,
28 global compilation of 6,814 georeferenced Ksat measurements from the literature across the globe
29 were used. The accuracy assessment results based on model cross-validations with re-fitting show
30 a concordance correlation coefficient of 0.79 and root mean square error of 0.72 (in $\log_{10}K_{sat}$
31 given in cm/day). The generated maps of Ksat represent spatial patterns of the vegetation-induced
32 soil structure formation and clay mineralogy, more distinctly than previous global maps of Ksat
33 such as computed with Rosetta 3 pedotransfer function. The validation of the model indicates
34 that Ksat could be more accurately modeled using covariate-based Geo Transfer Functions (CoGTFs)
35 that harness spatially distributed surface and climate attributes, compared to pedotransfer func-
36 tions that rely only on soil information.

37 Plain Language Summary

38 The soil saturated hydraulic conductivity Ksat defines how fast water can infiltrate and per-
39 colate through the soil. To model water flow at large scale, accurate maps of Ksat are needed. Usu-
40 ally, Ksat is not measured directly but deduced from well known basic soil properties (soil tex-
41 ture, packing density). But these estimates neglect the influence of vegetation and climate on for-
42 mation of soil structures that control Ksat. To improve predictions of Ksat, we use a new spa-
43 tially referenced Ksat data collection and apply Machine Learning to find correlations between
44 Ksat and other properties (soil information, terrain, climate and vegetation). These correlations
45 are then implemented at global scale using maps of all relevant properties (so called ‘*covariates*’
46 that were measured by remote sensing). We called this new approach to predictive soil mapping
47 the “*Covariate-based Geotransfer functions*” (CoGTF) to highlight the difference to other maps
48 that neglect spatial correlation with soil formatting properties and are based only on soil infor-
49 mation (so called “*pedotransfer functions*” or PTFs). We show that the new maps based on CoGTF
50 perform better than approaches based on PTFs.

51 1 Introduction

52 The description of water, energy, and carbon fluxes between the land surface and the at-
53 mosphere relies heavily on the availability of soil hydraulic data (Gutmann & Small, 2007; Fashi
54 et al., 2016; Montzka et al., 2017). A prominent soil hydraulic property is the soil saturated hy-
55 draulic conductivity (Ksat) that affects the partitioning of rainfall between runoff and infiltration
56 (Zimmermann et al., 2013), and plays a critical role in a variety of hydrological and climatolog-
57 ical applications (Gutmann & Small, 2007; Or, 2019; Fatichi et al., 2020). At global scale, maps

58 of soil hydraulic properties at ever increasing resolution are required for building Land Surface
59 Models (LSMs) (Montzka et al., 2017).

60 For large scale applications (regional and global), soil hydraulic parameters are often es-
61 timated from easy-to-measure soil properties (e.g., texture, organic content, bulk density) by means
62 of pedotransfer functions (PTFs) (Bouma, 1989; Santra & Das, 2008). PTFs are usually devel-
63 oped for specific geographic regions thus only representing local conditions of soil forming pro-
64 cesses (e.g. Tomasella & Hodnett, 1998; Wösten et al., 1999; Nemes et al., 2005; Saxton & Rawls,
65 2006; Jorda et al., 2015; Khlosi et al., 2016). This hinders their transferability across large ge-
66 ographical regions (Vereecken et al., 2016). In addition, PTFs generally ignore soil structure and
67 pedogenic information and rely heavily on soil textural information (Fatichi et al., 2020), lim-
68 iting their applicability in soils characterized by aggregation and formation of biopores. More-
69 over, PTFs are generally defined as a function of clay content, without consideration of the ef-
70 fect of different clay minerals on soil hydraulic properties (Hodnett & Tomasella, 2002). Dai et
71 al. (2019) have recently produced 1–km resolution global maps of soil hydraulic properties (and
72 thermal soil conductivity) using the median values of multiple PTFs to estimate Ksat. Likewise,
73 Y. Zhang and Schaap (2017) have developed a global map of van Genuchten parameters and Ksat
74 based on the Rosetta 3 PTF (an extension of Schaap et al., 2001), making use of three data sets
75 from North America and Europe (i.e., Rawls et al., 1982; Ahuja et al., 1989) and UNSODA (Un-
76 saturated Soil Hydraulic Database) as described in Leij et al. (1996) and Nemes et al. (2001) and
77 employing Artificial Neural Network and bootstrap sampling.

78 Maps produced by Dai et al. (2019) and Y. Zhang and Schaap (2017) are limited by the small
79 number and unevenly distributed Ksat measurements ($N = 1306$) used for model training and
80 large spatial gaps i.e. missing training points in tropics. Moreover, the training points used to pro-
81 duce estimates of Ksat were usually dominated by particular land use and land cover, mainly col-
82 lected in arable land. Furthermore, only a limited set of basic soil variables (i.e., bulk density and
83 texture) was employed in the derivation of the Rosetta 3 map (Y. Zhang & Schaap, 2019), while
84 several studies have shown that also other soil properties such as organic carbon, soil depth and
85 pH may increase accuracy of PTFs (Wösten et al., 1999; Mayr & Jarvis, 1999; Tóth et al., 2015).
86 The availability of highly resolved remote sensing (RS) and landscape covariates offer new op-
87 portunities for injecting new and local information into the modeling of Ksat. Examples of the
88 potential usefulness of such covariates are reported by Obi et al. (2014) that developed a PTF us-
89 ing terrain attributes for many soil hydraulic properties; Sharma et al. (2006) combined PTFs with
90 vegetation and topography indices; Jana and Mohanty (2011) showed that the introduction of to-
91 pographic attributes (i.e., Digital Elevation Model, DEM) and information on vegetation (i.e., Leaf
92 Area Index, LAI) along with *in situ* soil basic properties could improve predictions of soil hy-
93 draulic properties.

94 Many of the recent PTFs use Machine Learning (ML) algorithms to quantify the relations
95 between hydraulic properties and various covariates (Schaap et al., 2001; Jana & Mohanty, 2011;
96 Araya & Ghezzehei, 2019). In this paper, we hypothesize that Ksat predictions could be improved
97 using a combination of soil variables and remote sensing covariate layers integrated by using ma-
98 chine learning (ML) framework. We profit from the advancement in remote sensing techniques
99 (providing spatial information on different ecological parameters with unprecedented resolution)
100 to improve the predictions for soil hydraulic parameters and bridge the gap between site-specific

101 soil properties and landscape variability. We merge concepts of predictive soil mapping with a
 102 large data set of Ksat measurements and local information (soil, vegetation, climate) into covariate-
 103 based “*Geo Transfer Functions*” (CoGTFs) to generate global estimates of Ksat values (to high-
 104 light the impact of Geo-referencing soil properties and RS-covariates we use the term GTF and
 105 not PTF). We compare mapping accuracy using global and local/regional assessment including
 106 visual interpretation of produced spatial predictions. We show how this method (providing novel
 107 covariate-based maps of Ksat) could be used to overcome some of the limitations of traditional
 108 PTFs.

109 Our specific objectives are:

- 110 1. to improve accuracy and spatial detail of global Ksat maps by harnessing the state-of-the-
 111 art global remote sensing data products at 1 km spatial resolution,
- 112 2. to generate global maps of Ksat at different soil depths (0, 30, 60 and 100 cm),
- 113 3. to identify the key environmental variables explaining the spatial distribution of Ksat.

114 We first describe the model training for Ksat mapping using a random forest ML algorithm,
 115 and then compare the results against maps generated with Rosetta 3 and the map shown in Dai
 116 et al. (2019). Note that for a detailed comparison of global maps, we focus on Rosetta 3 because
 117 the map in Dai et al. (2019) is heavily influenced by the application of a different soil textural
 118 map (see Supplementary Information file). Then, we validated the CoGTF map, Rosetta 3 map
 119 and the map of Dai et al. (2019) with independent dataset. We finally show the importance of us-
 120 ing RS covariates to capture spatial patterns and improve the accuracy of soil hydraulic proper-
 121 ties.

122 2 MATERIALS AND METHODS

123 2.1 Covariate-based Geo Transfer Functions (CoGTF) framework

124 We propose here an integrated Predictive Soil Modeling (PSM) framework where soil vari-
 125 ables are combined with RS-based covariates using random forest method (Figure 1). We refer
 126 to this approach as the “*Covariate-based Geo Transfer Functions*” (CoGTF) framework and en-
 127 visage it as a combination of traditional PTF approach and purely data science approach where
 128 RS-based covariates are used to map patterns in soil properties. The CoGTF framework follows
 129 six principal steps:

- 130 1. Prepare georeferenced dataset of response variable (Ksat),
- 131 2. Overlay training points and covariates (including predictions of basic soil properties), and
 132 produce a regression matrix,
- 133 3. Optimize the hyper-parameters in the random forest approach (`mtry`),
- 134 4. Fit the random forest model,
- 135 5. Evaluate the performance of the Ksat model,
- 136 6. Produce spatial predictions of Ksat.

137 A central hypothesis in this study is that spatial and climatic covariates could be harnessed
 138 to improve the global mapping of Ksat (Jana & Mohanty, 2011). The basis for such hypothesis

139 is the dominant role of climate, topography, and vegetation in soil formation and thus in shap-
 140 ing local hydraulic transport properties. For each location with Ksat measurement, the values of
 141 the remote sensing covariates were extracted together with modeled soil information from Open-
 142 LandMap.org. We implement the spatial predictions and the creation of Ksat maps in the R en-
 143 vironment (R Core Team, 2013) for statistical computing and provide code examples via the [https://](https://github.com/ETHZ-repositories/Ksat_mapping_2020/)
 144 github.com/ETHZ-repositories/Ksat_mapping_2020/.

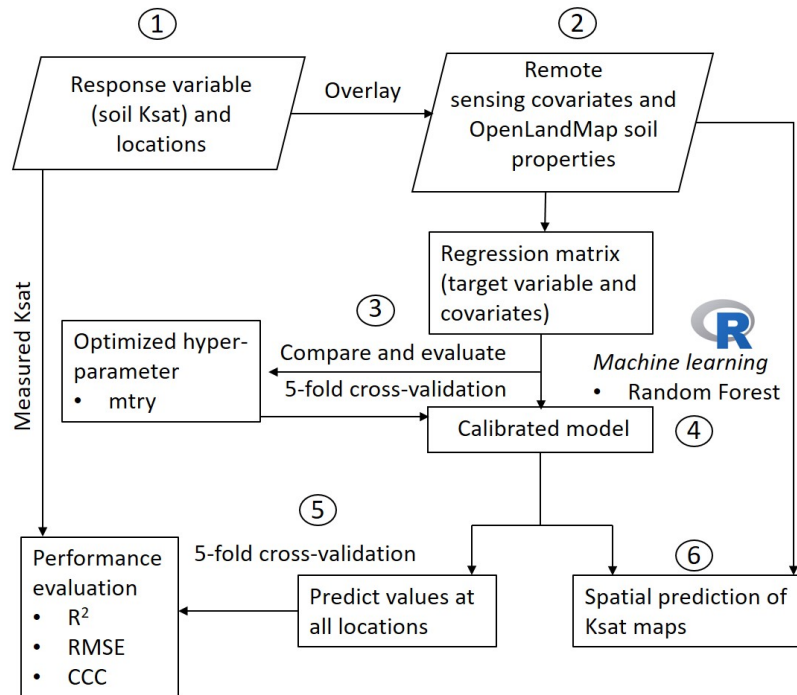


Figure 1. Computational workflow used to generate the soil Ksat map. See text for more details about the specific steps.

145 After extracting all covariates, a regression matrix was formed, and the best hyperparam-
 146 eter (`mtry`) was computed by five-fold cross-validation, using the R packages '`caret`' version 6.0-
 147 85 (Kuhn, 2012) and '`ranger`' version 0.12.1 (Wright & Ziegler, 2015). Then, log-transformed
 148 (\log_{10}) Ksat was modeled as a function of depth using random forest (RF) algorithm.

149 2.2 Training point data

150 Our first task was to enlarge the Ksat measurement database beyond the $\approx 1,300$ values used
 151 to train Rosetta 3 by compiling available and georeferenced Ksat values from the literature. The
 152 Ksat values were log-transformed (\log_{10} Ksat) and cm/day was selected as a standardized unit.
 153 A detailed description of the data collection and processing is provided in Gupta et al. (2020).
 154 We managed to compile a total of 13,267 samples coming from 1,910 sites across the globe. Most
 155 training data are from the USA, followed by Europe, Asia, South America, Africa, and Australia
 156 as shown in Figure 2. The collected Ksat database (SoilKsatDB) includes both field ($N = 4,460$)
 157 and lab ($N = 8,807$) measurements.

158 To limit the over-representation of Florida (mainly arable land not representative of soils
 159 with natural vegetation), we randomly selected approximately only 1% of the 6,532 Florida sam-
 160 ples, so that a total of 6,814 Ksat values were finally used for Ksat mapping. This resulted in ge-
 161 ographical balance between other national data sets (the effect of this selection of Florida data
 162 is discussed in Supplementary information file).

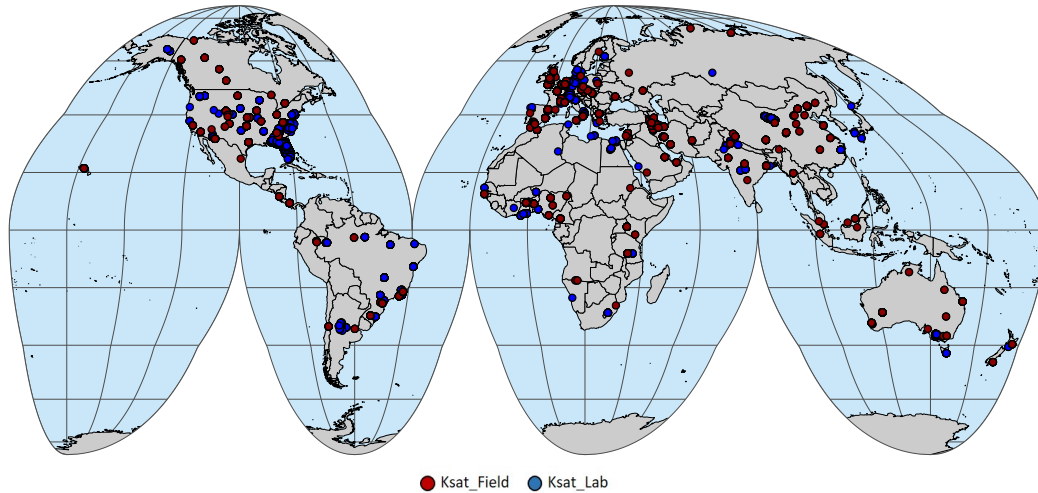


Figure 2. Spatial distribution of measured Ksat values (6,814 samples in total) used to produce the global Ksat map. Colors refer to laboratory (red) and field (blue) measurements. The map is presented in the Goode equal-area homolosine projection. For more details and access to the Ksat data see Gupta et al. (2020).

163 2.3 Soil and environmental covariates

164 As environmental and soil covariate layers for Ksat modeling at global scale, we used global
 165 maps of soil properties (sand, clay, and bulk density) and other 24 RS-based covariates available
 166 from <https://openlandmap.org/>. These were selected to represent ecological conditions es-
 167 sential in soil-forming processes according to Jenny (1994). The covariates can be divided into
 168 five groups:

- 169 1. *Climate-based covariates*, including mean annual precipitation, temperature, temperature
 170 seasonality, maximum temperature of warmest month, minimum temperature of coldest
 171 month, precipitation of wettest month, precipitation of driest month (Chelsa products, Karger
 172 et al., 2017), cloud fraction (Wilson & Jetz, 2016), diffuse irradiation, direct irradiation,
 173 annual land surface temperature, monthly precipitation and its standard deviation (Brocca
 174 et al., 2019).
- 175 2. *Digital terrain model (DTM)-based covariates* (Yamazaki et al., 2017), including land-
 176 scape metrics (such as slope, aspect, topographic wetness index) derived from SAGA GIS
 177 (Conrad et al., 2015) and landform classification and lithological maps.
- 178 3. *Surface reflectance-based covariates*, including surface reflectance from Landsat and MODIS
 179 dataset for different wavelength bands (Hansen et al., 2013), snow probability (Buchhorn
 180 et al., 2017) and regularly flooded wetlands (Tootchi et al., 2019).

- 181 4. *Vegetation-based covariate*, represented by the annual fraction of absorbed photosynthetically active radiation (FAPAR), averaged over the 2014-2019 period.
- 182
- 183 5. *Basic soil properties*, comprising sand, clay content and bulk density for different soil depths (matching the sampling depth of Ksat), which were obtained from OpenLandMap (Hengl et al., 2017). Soil depth is used as a covariate to model the change of Ksat with depth (the methodology to use depth as a covariate is described in Hengl & MacMillan, 2019).
- 184
- 185
- 186

187 A detailed list and description of all the covariates is provided in Table S1 in the Supplementary Information (SI). All covariate maps were resampled to the standard grid at a spatial resolution of 1 km covering latitudes between -62.0 and 87.37. We did not map Antarctica as this continent is dominantly covered with permanent ice and lacks training points.

188

189

190

191 2.4 Evaluating the performance of Ksat predictive models

192 The model-fitting results were evaluated using out of bag (OOB) error reported by the ranger package by default. A bootstrap sampling is used to construct each tree in the random forest and different bootstrap samples are used for each tree containing approximately 2/3 of the total observations. The samples not used in the bootstrap samples are called out-of-bag (OOB) samples (sub-dataset) (Peters et al., 2007; Rad et al., 2014). The relative importance of the covariates was assessed by the increase in node purity. It is calculated using gini criterion from all the splits (in our case 200 splits) in the forest based on a particular variable (Breiman, 2001; Rodrigues & de la Riva, 2014).

193

194

195

196

197

198

199

200 The performance of the Ksat model was evaluated using 5-fold cross-validation. This means that models were refitted 5 times using 80% of the data and the predictions for remaining 20% estimated using these models were compared with observations. The process was repeated three times to produce stable results. The final results are shown using hexbin plot with the LOWESS (Locally Weighted Scatterplot Smoothing) line to present the conditional bias of the Ksat values. The accuracy of the cross-validation predictions was evaluated using bias (mean error), root mean square error (RMSE), coefficient of determination (R^2) and concordance correlation coefficient (CCC).

201

202

203

204

205

206

207

208 Bias and RMSE are defined by:

$$bias = \sum_{i=1}^n \frac{(y_i - \hat{y}_i)}{n} \quad (1)$$

$$RMSE = \sqrt{\sum_{i=1}^n \frac{(\hat{y}_i - y_i)^2}{n}} \quad (2)$$

209 where y and \hat{y} are observed and predicted values and n is the total number of cross-validation points.

210 R^2 is defined as:

$$R^2 = \left[1 - \frac{SSE}{SST} \right] \% \quad (3)$$

211 where SSE is the sum of squared errors between the cross-validation predictions \hat{y} and the mea-
 212 surements y , and SST is the total sum of squares (proportional to variance of measurements). A
 213 coefficient of determination equal to 1 indicates that variance of the prediction errors is equal to
 214 zero but the bias may differ from zero.

215 In addition, Concordance Correlation Coefficient (CCC) (as measure of the agreement be-
 216 tween observed and predicted Ksat values) of cross validation (CV) (Lawrence & Lin, 1989) is
 217 given by:

$$CCC = \frac{2 \cdot \rho \cdot \sigma_{\hat{y}} \cdot \sigma_y}{\sigma_{\hat{y}}^2 + \sigma_y^2 + (\mu_{\hat{y}} - \mu_y)^2} \quad (4)$$

218 where $\mu_{\hat{y}}$ and μ_y are predicted and observed means, $\sigma_{\hat{y}}$ and σ_y are predicted and ob-
 219 served variances and ρ is the Pearson correlation coefficient between predicted and observed val-
 220 ues. CCC is equal to 1 for perfect model.

221 **2.5 Comparison of accuracy of Ksat maps: CoGTF, Rosetta 3 and the map of Dai** 222 **et al. (2019)**

223 The accuracy of the predictions of Ksat by the three approaches was evaluated with a sub-
 224 set of the Ksat database that was selected in the following way: First, the surface of the Earth was
 225 divided into blocks of 5 degrees as shown in Figure S1 in the SI. For fair comparison, Ksat mea-
 226 surements in blocks in North America or Europe were dropped because Rosetta 3 was mostly
 227 calibrated with data from these regions (2525 Ksat values were outside of these regions). Then
 228 we randomly selected blocks until about 20% of the remaining Ksat measurements had been cho-
 229 sen. These 508 Ksat measurements formed the test set for which predictions were extracted from
 230 the Rosetta 3 and the Dai et al. (2019) maps. CoGTF predictions of Ksat were computed for these
 231 508 test observations. The accuracy of the predictions by the three approaches was then evalu-
 232 ated with the same criteria as used for cross-validation.

233 **3 Results**

234 **3.1 Model fitting and accuracy of modeled Ksat values**

235 The CoGTF model fitted the logarithms of the Ksat measurements reasonably well (out-
 236 of-bag RMSE = 0.73 (\log_{10} Ksat in cm/day) and $R^2 = 0.66$). Figure 3 shows the list of most im-
 237 portant covariates for Ksat modelling. The x -axis displays the average increase in node purity.
 238 The higher the value, the more important is a covariate. Figure 3 shows that sand content was found
 239 the most important covariate followed by elevation (important for soil formation and water flow),
 240 clay content, and bulk density. Climate covariates are dominating after the fifth covariate.

241 The results of the 5-fold cross-validation are presented in Figure 4a using hexbin density
 242 plots. For predictions of Ksat greater than equal to 10 cm/day the line of LOWESS falls onto the
 243 1:1-line, hence the predictions were conditionally unbiased here. A slight positive conditional
 244 bias is visible for predictions less than 10 cm/day where the LOWESS line is below the 1:1 line.
 245 CoGTF tended to overestimate small Ksat values, but this bias remains small. Hence, RF pre-
 246 dictions were both marginally and conditionally approximately unbiased. Cross-validation re-

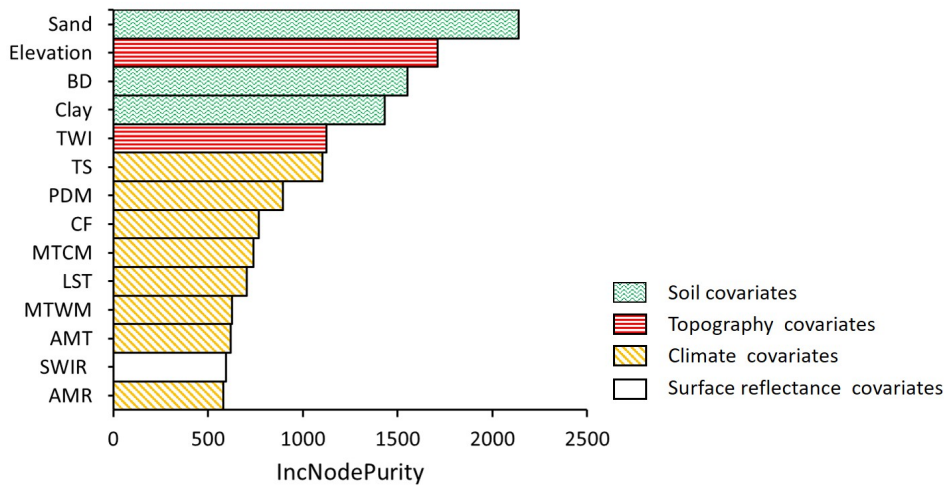


Figure 3. Importance of the covariates for modeling Ksat by a random forest model. The x-axis displays the average increase in node purity (the larger the value, the more important is a covariate). The 14 most important covariates are shown here: sand content, bulk density (BD), and clay content belong to soil covariates. Elevation and topographic wetness index (TWI) are topography covariates. Temperature seasonality (TS), precipitation of driest month (PDM), cloud fraction (CF), minimum temperature of coldest month (MTCM), annual average land surface temperature (LST), maximum temperature of warmest month (MTWM), mean annual temperature (AMT), and mean annual rainfall (AMR) belong to climate category. Shortwave infrared (SWIR) Landsat-7 band is from the surface reflectance group.

247 results show a reasonable overall model accuracy, with R^2 , CCC, and RMSE and bias equal to 0.66,
 248 0.79, 0.72, and 0.0039 (\log_{10} of Ksat in cm/day for RMSE and bias), respectively. The obser-
 249 vations were also correlated with Rosetta 3 Ksat map (for this comparison, a total of 5,255 sam-
 250 ples from shallow soil depth were selected out of 6,814 to compare with Rosetta 3 map for top
 251 15 cm) as shown in Figure 4b. RMSE and CCC was observed 1.23 and 0.12 (\log_{10} of Ksat in cm/day
 252 for RMSE), respectively.

253 3.2 Global map of Ksat

254 Global Ksat maps were produced for four soil depths (0, 30, 60, and 100 cm). Figure 5a
 255 shows the CoGTF map of Ksat at 0 cm soil depth, while results for other soil depths are provided
 256 in Figure S2 (SI). Ksat values in the top layer (0 cm depth) vary between 0.05 to 31,600 cm/day.
 257 High Ksat values were predicted for the equatorial belt and for parts of Russia and Canada, while
 258 low Ksat values were produced in East America, Europe and parts of Asia (mainly India and North-
 259 East part of China). In general, Ksat value decreased with depth, with the most significant reduc-
 260 tion observed in North America, South America, China, India, and Russia (see Figures S2-S3 in
 261 the SI). Figure 6 compares the probability distribution of the global Ksat map values with the dis-
 262 tribution of measured and fitted Ksat values for the 6,814 Ksat samples. Results show a more peaked
 263 distribution of global Ksat map compared to the measured and fitted Ksat at the sampling loca-
 264 tions. Both measured (red) and fitted \log_{10} Ksat showed the same mean values of 1.64 with stan-
 265 dard deviations 1.25 and 1.01, respectively, whereas the mean and standard deviation of global
 266 map were observed 1.99 and 0.30 respectively.

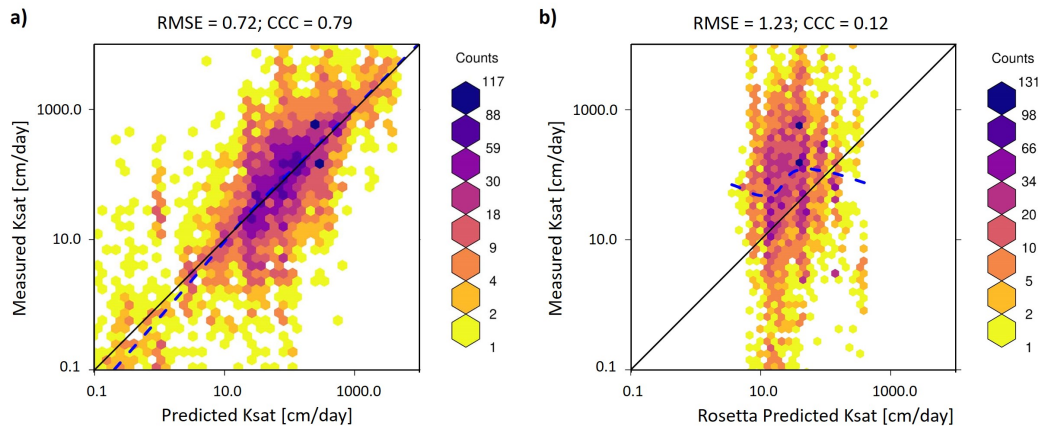


Figure 4. Accuracy plots based on cross-validation: (a) correlation between observations and cross-validation predictions of \log_{10} Ksat based on CoGTF model, (b) correlation between observations (0-30 cm soil depth) and Rosetta 3 predicted values from 0-15 cm map. The color codes the number of observations in each hexagonal pixel. The solid black line is 1:1 line and the blue dashed line is LOWESS curve (locally weighted scatterplot smoothing). The model accuracy of CoGTF was assessed using CCC (0.79) and RMSE (0.72). The RMSE and CCC between observations and Rosetta 3 predicted Ksat values were observed 1.23 and 0.12, respectively. The unit of RMSE is \log_{10} of Ksat in cm/day.

267

3.3 Comparison with Rosetta 3 global Ksat map

268

269

270

271

272

273

274

275

276

The CoGTF Ksat map is compared with the Rosetta 3 map (Y. Zhang & Schaap, 2019) in Figure 5. Note that there are different models of Rosetta 3 according to the soil information used to build the neural network: H1w (information on soil textural class), H2w (sand, silt, and clay percentage), H3w (sand, silt, and clay percentage plus bulk density), H4w (same information as H3w plus water content at 330 cm suction), and H5w (same as H3w plus water content at 330 cm and at 15,000 cm) (X. Zhang et al., 2019). As standard model H3w is often chosen (see map in Y. Zhang & Schaap, 2019) because information on water content at 330 cm and 15,000 cm is sparse at global scale compared to bulk density and soil texture information. For comparison with CoGTF, we chose H3w model as well.

277

278

279

280

281

282

283

284

285

The main differences between the CoGTF map and Rosetta 3 are the low Ksat values predicted by Rosetta 3 for tropical regions and the abrupt change in Rosetta 3 predictions in high latitude regions of Canada and Russia as a consequence of the strong sensitivity of Rosetta 3 predictions on bulk density. In general, lower Ksat values were observed in the Rosetta 3 map compared to the CoGTF map for most regions worldwide except the northern regions (Canada and Russia), while regions with coarser soils such as Sahara and middle East showed higher Ksat values in Rosetta 3. The lower values of Ksat in Rosetta 3 than the in CoGTF map is evident in Figure 6a. Medians of the common logarithm of Ksat (unit cm/day) were equal to 1.62 and 2.00, respectively (Figure 6b).

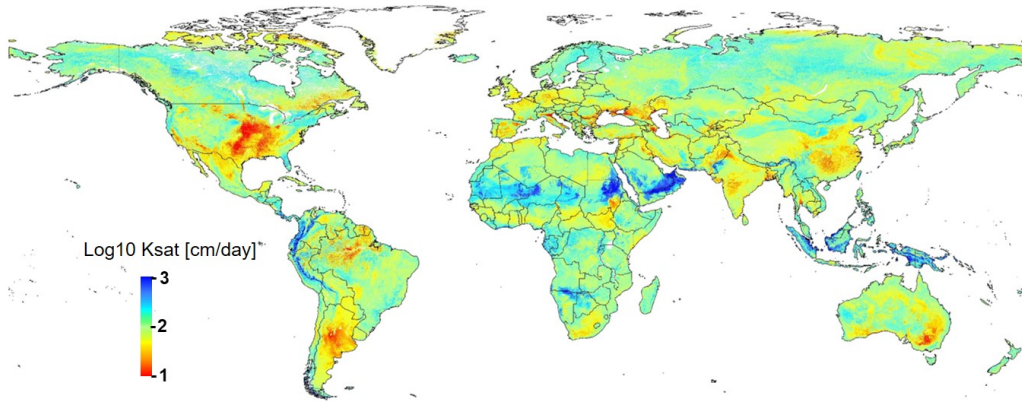
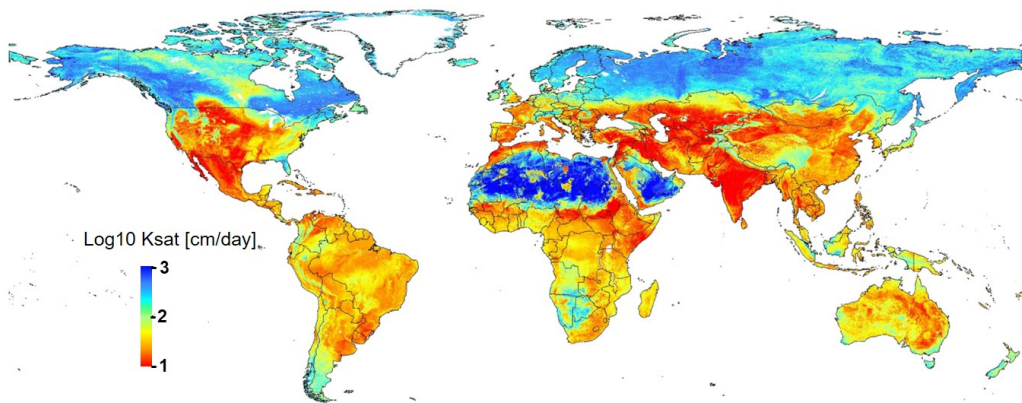
a) *CoGTF map (0 cm)*b) *Rosetta 3 map (0 cm)*

Figure 5. Visual comparison between (a) CoGTF Ksat map, and (b) map based on Rosetta 3 PTF. Ksat values predicted by Rosetta 3 were higher for sandy soils (Sahara) and in northern regions with smaller bulk density. The scale of the maps was truncated at minimum and maximum values of 10 and 1000 cm/day to show the significant variations in the maps

286

3.4 Validation of global Ksat maps

287

288

289

290

291

292

293

294

295

Table 1 shows the results of the comparison of the accuracy of Ksat predictions for the CoGTF, Rosetta 3 and Dai et al. (2019) maps (see Figures S7 and S8 for the map of Dai et al., 2019, with CoGTF map). A total of 372 Ksat samples out of the validation dataset with 508 samples (we selected samples with soil depth 0-30 cm) were compared with measured Ksat values and RMSE values of 1.02, 1.29, and 1.15 were computed (\log_{10} of Ksat in cm/day) for the CoGTF map, Rosetta 3, and Dai et al. (2019) map, respectively. The RMSE illustrates that CoGTF map showed better performance than the other maps. However, RMSE of 1 also shows that the precision is limited for CoGTF as well. The better performance of CoGTF is manifested in the much lower bias compared to the two other models.

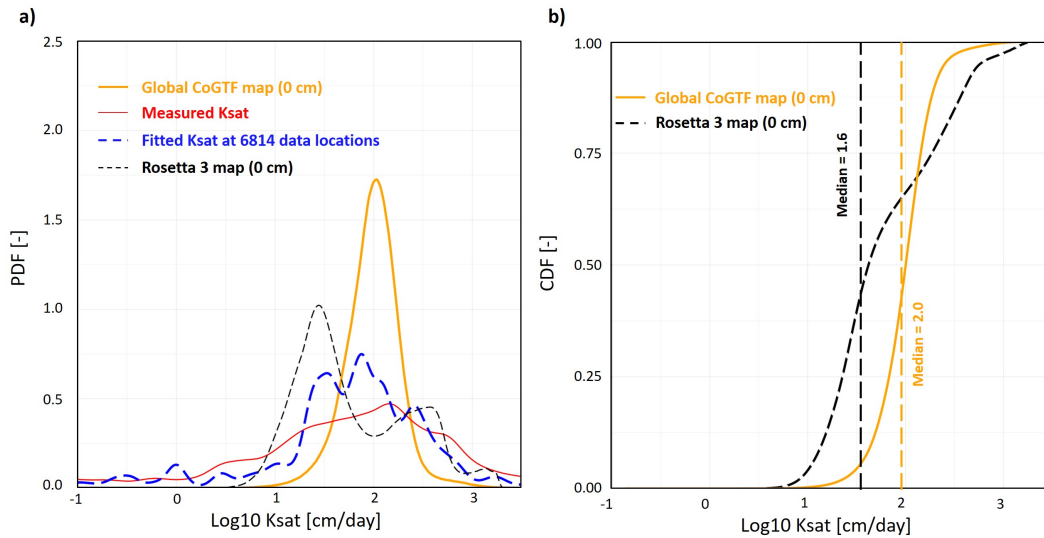


Figure 6. Difference in probability density functions (PDF): (a) between global CoGTF map (yellow) and Rosetta 3 (black) Ksat values at 0 cm depth, measured (red) and fitted (blue) Ksat values at the sampling sites, (b) cumulative distribution functions for Rosetta 3 map (black) and CoGTF map (yellow) for soil depth 0 cm.

Table 1. Root mean square error (RMSE) and bias of predictions of $\log_{10}(\text{Ksat})$ (units cm/day) for test data. A total of 372 Ksat sample points were selected to investigate the accuracy of Ksat predictions (0-30 cm soil depth were used). The negative signs in bias demonstrate that all three models underestimated Ksat values. The range shows the minimum and maximum values of 372 samples.

Models	Samples used	RMSE	bias	Extracted points range
CoGTF (0 -15 cm)	372	1.02	-0.19	0.85-2.60
Rosetta 3 (0 -15 cm)	372	1.29	-0.75	0.83-2.64
Dai et al. (2019) (0 -15 cm)	372	1.15	-0.51	0.68-2.30

296 4 Discussion

297 4.1 Characteristics of the CoGTF global Ksat maps

298 In this paper we have produced global estimates of Ksat by linking terrain, climate, veg-
 299 etation and soil spatial covariates to measured Ksat values, thus injecting local information usu-
 300 ally ignored by traditional PTFs. We refer to this approach as the Covariate-based Geo Trans-
 301 fer Functions (CoGTF) framework. The newly developed global CoGTF map of Ksat (Figure 5)
 302 shows high values in the Northern part of South America, the central part of Africa and South-
 303 east Asia (mainly Indonesia, Malaysia, Myanmar (Burma), Philippines, Singapore, and Thailand),
 304 most likely due to high rainfall, temperature, and vegetation. Our results shows (Figure 3) that
 305 rainfall, temperature and their variation are the most important climate covariates for the Ksat
 306 mapping (Shoji et al., 2006). This indicates that these climatic factors not only act as catalyst in
 307 soil chemical reactions but also determine the type and biomass of vegetation that is important
 308 for soil structure formation. This impact of vegetation on soil Ksat is in line with the research

309 by Niemeyer et al. (2014) who compared the leaf area index with Ksat and observed that high
 310 leaf area index increases the Ksat (with R-square = 0.33).

311 The central part of India, eastern part of Australia, and parts of China showed low Ksat val-
 312 ues due to the presence of high clay content that reduces the soil permeability (see as well dis-
 313 cussion on role of clay mineral type in section 4.2). The west part of North America, middle east
 314 countries (Tibet, Iran, Turkey), and northern parts of Algeria have low Ksat values that may be
 315 related to high elevation, low rainfall, less vegetation and thus less structure formation processes.
 316 Many studies have recognized the indirect influence of elevation on soil properties (Leij et al.,
 317 2004; Carter & Ciolkosz, 1991). Similarly, different land-use (forest or pasture) directly impact
 318 Ksat. Chandler et al. (2018) showed that forests had larger soil hydraulic conductivity than pas-
 319 tures.

320 Likewise, high values of Ksat up to around 100 to 300 cm/day are observed in desert re-
 321 gions such as Thar desert in India, northern and southern Africa, and central Australia, where dom-
 322 inating fractions of sand cause high water permeability. Similarly, Colombia and Peru showed
 323 high Ksat values due to high organic carbon content (Allison, 1973). Furthermore, high Ksat val-
 324 ues were observed in parts of Brazil that strongly decreased with depth. Similar results were re-
 325 ported by Belk et al. (2007). They conducted a study in the tropical forest of Brazil and measured
 326 the Ksat at various depths for different sites. The authors found that Ksat values at surface were
 327 mainly between 100 to 1000 cm/day and decreased with depth.

328 **4.2 Effect of clay type — active and inactive clay minerals**

329 Pedotransfer functions like Rosetta 3 and the ensemble of PTFs used in (Dai et al., 2019)
 330 to estimate soil hydraulic properties based on clay fraction and do not take into account the large
 331 differences in microstructure and hydration of different clay minerals. The remarkable spatial
 332 segregation in climatic regions of different clay minerals (see Ito & Wagai, 2017) and the differ-
 333 ent hydraulic properties of the clay minerals indicate that PTFs built for temperate regions with
 334 swelling clays cannot be applied for tropical regions with non-swelling clays (see Ottoni et al.,
 335 2018). In tropical soils, dense vegetation, and non-swelling (*‘inactive’*) kaolinite clay minerals
 336 result in higher conductivities (Hodnett & Tomasella, 2002) in contrast to PTFs that are trained
 337 with data from temperate soils with swelling (more *‘active’*) clays. This is further discussed for
 338 estimates relevant to Brazil shown in Figure 7.

339 In Figure 7, the CoGTF and Rosetta 3 Ksat maps are shown together with six covariates
 340 and clay mineral map. The Ksat values predicted with CoGTF are one order of magnitude higher
 341 than based on Rosetta 3. The difference stems from the dominant role of soil texture for Rosetta
 342 3 as illustrated with a black polygon in Figure 7: the polygon marks a region of high sand con-
 343 tent and low clay content that is manifested in relatively high values of Ksat for Rosetta 3, with
 344 values typical for temperate regions. For CoGTF, the conductivity in this *‘sand band’* is relatively
 345 low because other covariates and processes are more important. These lower values coincidence
 346 with low elevation. The important role of elevation in CoGTF is also manifested in the high Ksat
 347 values in the mountainous region in the south and the low Ksat values in the Amazon region. An-
 348 other reason for the lack of correlation between Ksat and texture for CoGTF in Brazil is the in-
 349 active clay mineral type (kaolinite) that does not limit Ksat the same way as in case of more ac-

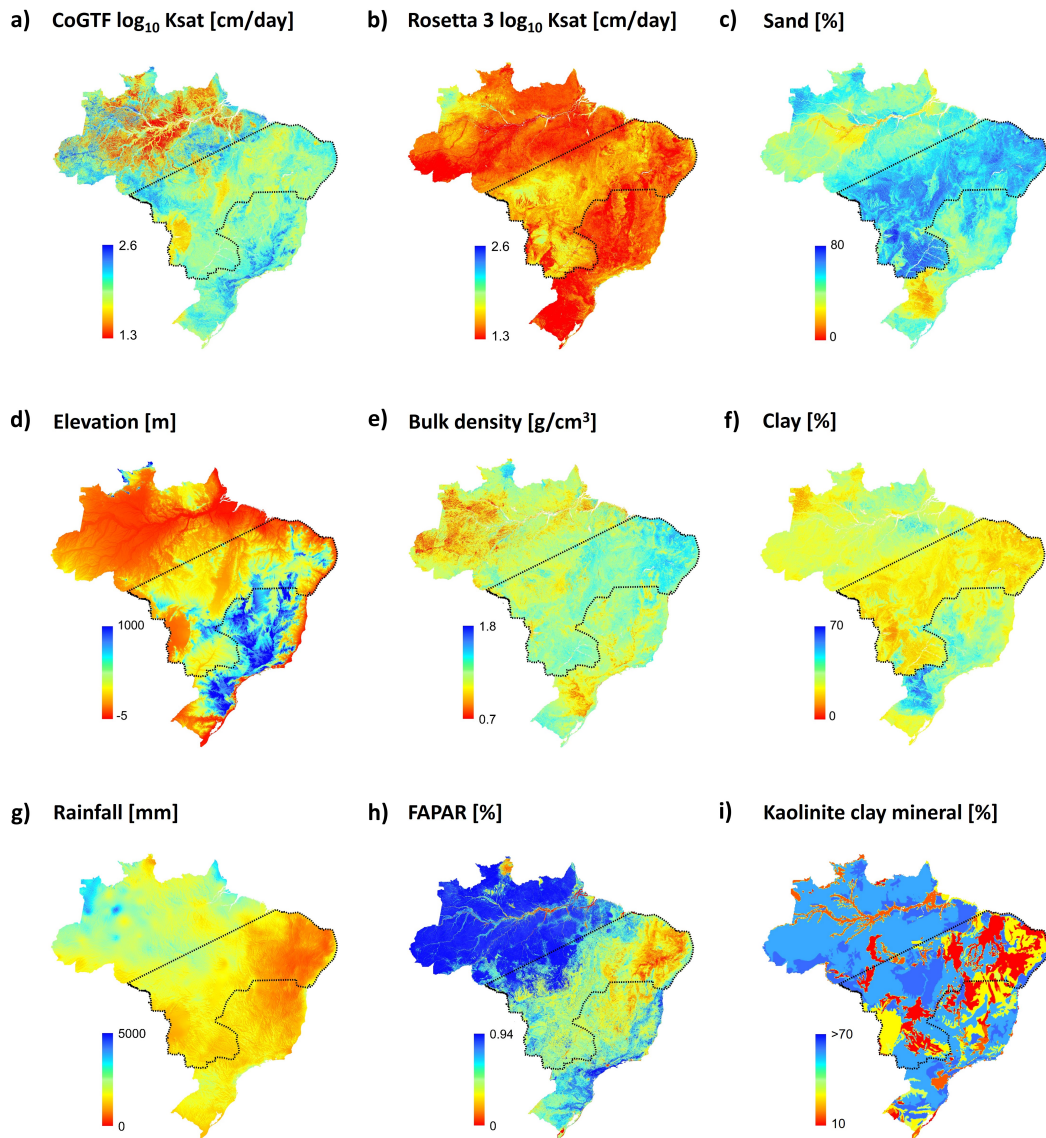


Figure 7. Predicted Ksat values for Brazil (a), spatial patterns of the Rosetta 3 Ksat map in \log_{10} cm/day (b) and of the first four most important covariates (c-f, see Figure 3): sand fraction (%), elevation (meters above sea level), bulk density (g/cm³) and clay fraction (%). Other covariates that are related to soil formation to link with Ksat are shown as well (g-i): mean annual rainfall (mm), Copernicus fraction of absorbed photosynthetically active radiation (FAPAR, values in %) and kaolinite (in %) clay mineral. The region with black polygon marks a region with high sand and low clay content that is expressed in Rosetta 3 as band of relatively high Ksat values. In contrast to Rosetta 3, CoGTF is not dominated by soil texture but takes into account covariates that are important for soil formation (here mainly the elevation).

350 tive clay in temperate regions. Precipitation and temperature are the main reasons for the strong
 351 chemical weathering of the rock and the formation of the non-swelling, kaolinite clay minerals
 352 (Montes et al., 2002). It is evident in Figure 7(g to i) that in the region with low rainfall and veg-
 353 etation kaolinite percentage is lower than other regions with high rainfall and vegetation.

354 In contrast to Brazil, India is a region with active (swelling) clay minerals. In contrast to
 355 the inactive kaolinite in Brazil, for the active clays in India, low Ksat values can be expected. Fig-
 356 ure S4a and S4i show the correlation between low Ksat values and high contents of smectite clay
 357 mineral. The low values of Ksat in central India directly relate to high clay content, low vege-
 358 tation biomass and low mean annual rainfall (see Figure S4 for covariates in SI). Figure S4b il-
 359 lustrates the Ksat values from Rosetta 3 for India. The patterns of high active clay fraction in In-
 360 dia is not captured by Rosetta 3 model. This might be the effect of considering only soil basic
 361 properties or using samples from only temperate region.

362 **4.3 Effects of information clustering — The Florida database example**

363 Out of 13,267 Ksat values, only 6,814 values were used for the Ksat mapping to avoid a
 364 distortion of the Ksat predictions by the many data from Florida. The dataset contained 6,532
 365 Ksat values from Florida but we used only 1% of these points for mapping. Figure S5a and S5b
 366 compares the map computed with all 13,267 Ksat measurements with the map trained on 6,814
 367 measurements. The difference between these maps (Figure S5c) showed a large impact on the
 368 sandy regions such as Sahara and center part of Africa and middle east with significantly higher
 369 Ksat values when all Florida points are included in the fitting. A similar effect was observed in
 370 parts of South America and Australia. On the other hand, the south of Africa and the higher north-
 371 ern latitudes showed higher Ksat values when only 1% of the Florida data was used.

372 **4.4 Improved model performance using remote sensing covariates**

373 As we described above, the RS (vegetation, topography, climatic) covariates could be used
 374 to harness the heterogeneity produced by these environmental variables as these factors shape
 375 clay activity and soil-forming processes that control saturated hydraulic conductivity (Ottoni et
 376 al., 2018; Hao et al., 2019). To investigate this effect of RS covariates in the predictions, we fit-
 377 ted the RF model only with soil properties or remote sensing covariates. The maps are shown in
 378 Figure S6a and S6b in the SI.

Table 2. Root mean square error (RMSE) and coefficient of determination (R^2) for different models.

Models	RMSE	R^2	Total covariates	Best mtry
CoGTF	0.72	0.66	28	6
Only soil covariates	0.75	0.63	4	2
Only RS covariates	0.73	0.65	24	16

379 Table 2 shows the RMSE and R^2 using different models where we used only soil covari-
 380 ates, only remote sensing covariates, and the CoGTF model. Remote sensing (RMSE = 0.73; R^2
 381 = 0.65) predicted the Ksat better than only soil covariates (RMSE = 0.75; R^2 = 0.63). Similarly,
 382 the CoGTF model showed lower RMSE (0.72) and higher R^2 (0.66) than only RS covariate. Hence,
 383 consideration of RS covariates in predicting hydraulic properties could increase the accuracy of
 384 the predictions of soil hydraulic properties compared to a model that is based only on soil infor-
 385 mation.

386 **4.5 Usage of the global CoGTF Ksat maps and future developments**

387 We observed that RMSE in the model validation for the CoGTF map was better than the
 388 other maps. However, RMSE with 1 (\log_{10} Ksat in units of cm/day) also shows that the preci-
 389 sion of even the CoGTF map is not so good. On the other hand, the bias for CoGTF map was much
 390 better than for the other maps. Although, the predictions are not so accurate, it shows the one step
 391 ahead in terms of improvement in the predictions using distributed Ksat dataset and considera-
 392 tion of RS covariates.

393 The global CoGTF maps can be used to extract the information of Ksat at different depths
 394 for local, regional, and global scale studies. On the local scale, these maps can be helpful in agro-
 395 nomic processes such as soil interpretation, water-plant relationships, and assessing soil suitabil-
 396 ity for agriculture. For regional and global scale, the maps could provide unique values to each
 397 pixel in watershed scale and Earth surface models and would enhance the heterogeneity and ac-
 398 curacy in the area. The maps could also be useful for the soil water management policies as guide-
 399 line to show where soil reclamation is required to reduce and enhance the hydraulic conductiv-
 400 ity.

401 The actual CoGTF map has a resolution of 1 km. This resolution may be improved in the
 402 near future considering various initiatives to estimate soil and RS information with higher res-
 403 olution. But independent of improved resolutions, subgrid information on Ksat may be required
 404 for a catchment when specific information on soil texture or vegetation type is available. For such
 405 applications, we are actually developing a parametric model of CoGTF so that Ksat can be es-
 406 timated as a linear combination of most important covariates.

407 **5 Conclusions**

408 Soil saturated hydraulic conductivity is an important soil property for the parameterization
 409 of Earth system and land surface models. The major limitations of currently available maps are
 410 that (1) they are developed using a limited number of Ksat measurements mainly from temper-
 411 ate regions, (2) they are derived only from basic soil properties thus ignoring the effect of biologically-
 412 induced soil structure as well as clay mineralogy, and (3) they are not benefiting from the wealth
 413 of local remote sensing (RS) covariates. Therefore, we proposed a new global map of Ksat ob-
 414 tained by linking the measured Ksat values (6,814 samples) with 24 remote sensing covariates
 415 and 3 soil properties (sand content, clay content and bulk density) to add local information on
 416 vegetation, climate, and topography. The new map combines georeferenced information of soil
 417 properties and remote sensing covariates and is called covariate-based Geo Transfer Functions
 418 (CoGTF) map. We used the random forest machine-learning algorithm to fit the Ksat models and
 419 the performance was assessed using CCC and RMSE which was computed using 5 fold cross-
 420 validation. The CCC and RMSE (in \log_{10} Ksat given in cm/day) were observed 0.79 and 0.72,
 421 respectively. The CoGTF global Ksat map was compared with the map calculated with the well
 422 known Rosetta 3 PTF and major differences between the two maps were found. Firstly, Ksat val-
 423 ues in Rosetta 3 were much lower for tropical regions compared to the CoGTF map. The trop-
 424 ical regions are expected to have rather high Ksat values due to intense soil formation processes
 425 and presence of more conductive clay minerals (kaolinite). The effects of active and inactive clay
 426 minerals on Ksat are captured in CoGTF map as formation of clay minerals are linked to precip-

427 itation, temperature and dense vegetation. Secondly, in CoGTF there is no abrupt change in Ksat
 428 as shown in Rosetta 3 map for the higher latitude regions such as Canada and Russia. This large
 429 contrast is related to a change in bulk density that is dominant in Rosetta 3. In CoGTF, RS co-
 430 variates pattern cover this contrast. Furthermore, the CoGTF map, Rosetta 3 map, and the map
 431 of Dai et al. (2019) were validated using test data that were not used to calibrate the models, and
 432 the result showed that the CoGTF map performed better than the other models. Consequently,
 433 we propose to transition from PTFs based only on soil texture and bulk density to spatial-association
 434 of climate and vegetation covariates ("GTFs") to estimate Ksat. The study provides a blueprint
 435 for how georeferenced covariates could be used within the machine learning framework to im-
 436 prove Ksat predictive mapping. Moreover, the resulting CoGTF global maps are readily updat-
 437 able as more information becomes available (covariates of measured Ksat).

438 **Acknowledgments**

439 The study was supported by ETH Zurich (Grant ETH-18 18-1). We would like to thank Zhong-
 440 wang Wei, Samuel Bickel and Simone Fatichi (ETH Zurich) for insightful discussions. The data
 441 sets produced in this study are available at <https://doi.org/10.5281/zenodo.3934853>.

442 **References**

- 443 Ahuja, L., Cassel, D., Bruce, R., & Barnes, B. (1989). Evaluation of spatial distribution of
 444 hydraulic conductivity using effective porosity data. *Soil Science*, 148(6), 404–411.
- 445 Allison, F. E. (1973). *Soil organic matter and its role in crop production*. Elsevier.
- 446 Araya, S. N., & Ghezzehei, T. A. (2019). Using machine learning for prediction of sat-
 447 urated hydraulic conductivity and its sensitivity to soil structural perturbations. *Water*
 448 *Resources Research*, 55(7), 5715–5737.
- 449 Belk, E. L., Markewitz, D., Rasmussen, T. C., Carvalho, E. J. M., Nepstad, D. C., & David-
 450 son, E. A. (2007). Modeling the effects of throughfall reduction on soil water content
 451 in a brazilian oxisol under a moist tropical forest. *Water Resources Research*, 43(8).
- 452 Bouma, J. (1989). Using soil survey data for quantitative land evaluation. In *Advances in soil*
 453 *science* (pp. 177–213). Springer.
- 454 Breiman, L. (2001). Random forests. *Machine learning*, 45(1), 5–32.
- 455 Brocca, L., Filippucci, P., Hahn, S., Ciabatta, L., Massari, C., Camici, S., . . . Wagner, W.
 456 (2019). SM2RAIN-ASCAT (2007–2018): Global daily satellite rainfall from ASCAT
 457 soil moisture. *Earth Syst. Sci. Data Discuss*, 1–31.
- 458 Buchhorn, M., Bertels, L., Smets, B., Lesiv, M., & Wur, N. (2017). Copernicus Global Land
 459 Operations “Vegetation and Energy”. *Copernicus Global Land Operations “Vegetation*
 460 *and Energy*.
- 461 Carter, B. J., & Ciolkosz, E. J. (1991). Slope gradient and aspect effects on soils developed
 462 from sandstone in pennsylvania. *Geoderma*, 49(3-4), 199–213.
- 463 Chandler, K., Stevens, C., Binley, A., & Keith, A. (2018). Influence of tree species and forest
 464 land use on soil hydraulic conductivity and implications for surface runoff generation.
 465 *Geoderma*, 310, 120–127.
- 466 Conrad, O., Bechtel, B., Bock, M., Dietrich, H., Fischer, E., Gerlitz, L., . . . Böhner, J.
 467 (2015). System for automated geoscientific analyses (saga) v. 2.1.4. *Geoscientific*

- 468 *Model Development*, 8(7), 1991–2007. doi: 10.5194/gmd-8-1991-2015
- 469 Dai, Y., Xin, Q., Wei, N., Zhang, Y., Shanguan, W., Yuan, H., . . . Lu, X. (2019). A global
470 high-resolution dataset of soil hydraulic and thermal properties for land surface model-
471 ing. *Journal of Advances in Modeling Earth Systems*.
- 472 Fashi, F. H., Gorji, M., & Shorafa, M. (2016). Estimation of soil hydraulic parameters for
473 different land-uses. *Modeling Earth Systems and Environment*, 2(4), 1–7.
- 474 Fatichi, S., Or, D., Walko, R., Vereecken, H., Young, M. H., Ghezzehei, T. A., . . . Avissar,
475 R. (2020). Soil structure is an important omission in earth system models. *Nature*
476 *Communications*, 11.
- 477 Gupta, S., Hengl, T., Lehmann, P., Bonetti, S., & Or, D. (2020, April). SoilKsatDB: a global
478 compilation of soil saturated hydraulic conductivity measurements.
479 doi: 10.5281/zenodo.3752721
- 480 Gutmann, E. D., & Small, E. E. (2007). A comparison of land surface model soil hydraulic
481 properties estimated by inverse modeling and pedotransfer functions. *Water Resources*
482 *Research*, 43(5).
- 483 Hansen, M. C., Potapov, P. V., Moore, R., Hancher, M., Turubanova, S. A., Tyukavina, A.,
484 . . . Townshend, J. R. G. (2013). High-resolution global maps of 21st-century forest
485 cover change. *Science*, 342(6160), 850–853. doi: 10.1126/science.1244693
- 486 Hao, M., Zhang, J., Meng, M., Chen, H. Y., Guo, X., Liu, S., & Ye, L. (2019). Impacts of
487 changes in vegetation on saturated hydraulic conductivity of soil in subtropical forests.
488 *Scientific reports*, 9(1), 1–9.
- 489 Hengl, T., de Jesus, J. M., Heuvelink, G. B., Gonzalez, M. R., Kilibarda, M., Blagotić, A.,
490 . . . others (2017). Soilgrids250m: Global gridded soil information based on machine
491 learning. *PLoS one*, 12(2), e0169748.
- 492 Hengl, T., & MacMillan, R. A. (2019). *Predictive Soil Mapping with R*. Lulu. com.
- 493 Hodnett, M., & Tomasella, J. (2002). Marked differences between van genuchten soil
494 water-retention parameters for temperate and tropical soils: a new water-retention
495 pedo-transfer functions developed for tropical soils. *Geoderma*, 108(3-4), 155–180.
- 496 Ito, A., & Wagai, R. (2017). Global distribution of clay-size minerals on land surface for bio-
497 geochemical and climatological studies. *Scientific data*, 4, 170103.
- 498 Jana, R. B., & Mohanty, B. P. (2011). Enhancing ptf's with remotely sensed data for multi-
499 scale soil water retention estimation. *Journal of hydrology*, 399(3-4), 201–211.
- 500 Jenny, H. (1994). *Factors of soil formation: a system of quantitative pedology*. Courier Cor-
501 poration.
- 502 Jorda, H., Bechtold, M., Jarvis, N., & Koestel, J. (2015). Using boosted regression trees to
503 explore key factors controlling saturated and near-saturated hydraulic conductivity.
504 *European Journal of Soil Science*, 66(4), 744–756.
- 505 Karger, D. N., Conrad, O., Böhner, J., Kawohl, T., Kreft, H., Soria-Auza, R. W., . . . Kessler,
506 M. (2017). Climatologies at high resolution for the earth's land surface areas. *Scien-
507 tific data*, 4, 170122.
- 508 Khlosi, M., Alhamdoosh, M., Douaik, A., Gabriels, D., & Cornelis, W. (2016). Enhanced
509 pedotransfer functions with support vector machines to predict water retention of
510 calcareous soil. *European Journal of Soil Science*, 67(3), 276–284.

- 511 Kuhn, M. (2012). The caret package. *R Foundation for Statistical Computing, Vienna, Aus-*
512 *tria. URL [https://cran.r-project.org/package= caret](https://cran.r-project.org/package=caret).*
- 513 Lawrence, I., & Lin, K. (1989). A concordance correlation coefficient to evaluate repro-
514 ducibility. *Biometrics*, 255–268.
- 515 Leij, F., Alves, W., Van Genuchten, M. T., & Williams, J. (1996). The unsoda unsaturated
516 soil hydraulic database; user’s manual, version 1.0. *Rep. EPA/600/R-96*, 95, 103.
- 517 Leij, F., Romano, N., Palladino, M., Schaap, M. G., & Coppola, A. (2004). Topographical at-
518 tributes to predict soil hydraulic properties along a hillslope transect. *Water Resources*
519 *Research*, 40(2).
- 520 Mayr, T., & Jarvis, N. (1999). Pedotransfer functions to estimate soil water retention param-
521 eters for a modified brooks–corey type model. *Geoderma*, 91(1-2), 1–9.
- 522 Montes, C. R., Melfi, A. J., Carvalho, A., Vieira-Coelho, A. C., & Formoso, M. L. (2002).
523 Genesis, mineralogy and geochemistry of kaolin deposits of the jari river, amapá state,
524 brazil. *Clays and Clay Minerals*, 50(4), 494–503.
- 525 Montzka, C., Herbst, M., Weihermüller, L., Verhoef, A., & Vereecken, H. (2017). A global
526 data set of soil hydraulic properties and sub-grid variability of soil water retention and
527 hydraulic conductivity curves. *Earth System Science Data*, 9(2), 529–543.
- 528 Nemes, A., Rawls, W. J., & Pachepsky, Y. A. (2005). Influence of organic matter on the es-
529 timation of saturated hydraulic conductivity. *Soil Science Society of America Journal*,
530 69(4), 1330–1337.
- 531 Nemes, A., Schaap, M., Leij, F., & Wösten, J. (2001). Description of the unsaturated soil hy-
532 draulic database unsoda version 2.0. *Journal of Hydrology*, 251(3-4), 151–162.
- 533 Niemeyer, R., Fremier, A. K., Heinse, R., Chávez, W., & DeClerck, F. A. (2014). Woody
534 vegetation increases saturated hydraulic conductivity in dry tropical Nicaragua. *Vadose*
535 *Zone Journal*, 13(1).
- 536 Obi, J., Ogban, P., Ituen, U., & Udoh, B. (2014). Development of pedotransfer functions for
537 coastal plain soils using terrain attributes. *Catena*, 123, 252–262.
- 538 Or, D. (2019). The tyranny of small scales—on representing soil processes in global land sur-
539 face models. *Water Resources Research*.
- 540 Ottoni, M. V., Ottoni Filho, T. B., Schaap, M. G., Lopes-Assad, M. L. R., & Rotunno Filho,
541 O. C. (2018). Hydrophysical database for Brazilian soils (HYBRAS) and pedotransfer
542 functions for water retention. *Vadose Zone Journal*, 17(1).
- 543 Peters, J., De Baets, B., Verhoest, N. E., Samson, R., Degroeve, S., De Becker, P., & Huy-
544 brechts, W. (2007). Random forests as a tool for ecohydrological distribution mod-
545 elling. *ecological modelling*, 207(2-4), 304–318.
- 546 R Core Team. (2013). R: A Language and Environment for Statistical Computing [Computer
547 software manual]. Vienna, Austria. Retrieved from <http://www.R-project.org/>
- 548 Rad, M. R. P., Toomanian, N., Khormali, F., Brungard, C. W., Komaki, C. B., & Bogaert, P.
549 (2014). Updating soil survey maps using random forest and conditioned latin hyper-
550 cube sampling in the loess derived soils of northern iran. *Geoderma*, 232, 97–106.
- 551 Rawls, W. J., Brakensiek, D. L., & Saxton, K. (1982). Estimation of soil water properties.
552 *Transactions of the ASAE*, 25(5), 1316–1320.
- 553 Rodrigues, M., & de la Riva, J. (2014). An insight into machine-learning algorithms to
554 model human-caused wildfire occurrence. *Environmental Modelling & Software*, 57,

- 555 192–201.
- 556 Santra, P., & Das, B. S. (2008). Pedotransfer functions for soil hydraulic properties devel-
557 oped from a hilly watershed of eastern india. *Geoderma*, *146*(3-4), 439–448.
- 558 Saxton, K. E., & Rawls, W. J. (2006). Soil water characteristic estimates by texture and or-
559 ganic matter for hydrologic solutions. *Soil science society of America Journal*, *70*(5),
560 1569–1578.
- 561 Schaap, M. G., Leij, F. J., & Van Genuchten, M. T. (2001). Rosetta: A computer program for
562 estimating soil hydraulic parameters with hierarchical pedotransfer functions. *Journal*
563 *of hydrology*, *251*(3-4), 163–176.
- 564 Sharma, S. K., Mohanty, B. P., & Zhu, J. (2006). Including topography and vegetation at-
565 tributes for developing pedotransfer functions. *Soil Science Society of America Jour-*
566 *nal*, *70*(5), 1430–1440.
- 567 Shoji, S., Nanzyo, M., & Takahashi, T. (2006). Factors of soil formation: climate. as exem-
568 plified by volcanic ash soils. *Soils: Basic concepts and future challenges*. Cambridge
569 University Press, Cambridge, UK, 131–149.
- 570 Tomasella, J., & Hodnett, M. G. (1998). Estimating soil water retention characteristics from
571 limited data in brazilian amazonia. *Soil science*, *163*(3), 190–202.
- 572 Tootchi, A., Jost, A., & Ducharne, A. (2019). Multi-source global wetland maps combin-
573 ing surface water imagery and groundwater constraints. *Earth System Science Data*,
574 *11*, 189–220.
- 575 Tóth, B., Weynants, M., Nemes, A., Makó, A., Bilas, G., & Tóth, G. (2015). New genera-
576 tion of hydraulic pedotransfer functions for europe. *European journal of soil science*,
577 *66*(1), 226–238.
- 578 Vereecken, H., Schnepf, A., Hopmans, J. W., Javaux, M., Or, D., Roose, T., . . . others
579 (2016). Modeling soil processes: Review, key challenges, and new perspectives.
580 *Vadose zone journal*, *15*(5).
- 581 Wilson, A. M., & Jetz, W. (2016, 03). Remotely sensed high-resolution global cloud dy-
582 namics for predicting ecosystem and biodiversity distributions. *PLOS Biology*, *14*(3),
583 1-20. Retrieved from <http://dx.doi.org/10.1371/journal.pbio.1002415>
584 doi: 10.1371/journal.pbio.1002415
- 585 Wösten, J., Lilly, A., Nemes, A., & Le Bas, C. (1999). Development and use of a database of
586 hydraulic properties of european soils. *Geoderma*, *90*(3-4), 169–185.
- 587 Wright, M. N., & Ziegler, A. (2015). ranger: A fast implementation of random forests for
588 high dimensional data in c++ and r. *arXiv preprint arXiv:1508.04409*.
- 589 Yamazaki, D., Ikeshima, D., Tawatari, R., Yamaguchi, T., O’Loughlin, F., Neal, J. C., . . .
590 Bates, P. D. (2017). A high-accuracy map of global terrain elevations. *Geophysical*
591 *Research Letters*, *44*(11), 5844–5853.
- 592 Zhang, X., Zhu, J., Wendroth, O., Matocha, C., & Edwards, D. (2019). Effect of macro-
593 porosity on pedotransfer function estimates at the field scale. *Vadose Zone Journal*,
594 *18*(1).
- 595 Zhang, Y., & Schaap, M. G. (2017). Weighted recalibration of the Rosetta pedotransfer
596 model with improved estimates of hydraulic parameter distributions and summary
597 statistics (Rosetta3). *Journal of Hydrology*, *547*, 39–53.

- 598 Zhang, Y., & Schaap, M. G. (2019). Estimation of saturated hydraulic conductivity with pe-
599 dotransfer functions: A review. *Journal of Hydrology*, 575, 1011–1030.
- 600 Zimmermann, A., Schinn, D. S., Francke, T., Elsenbeer, H., & Zimmermann, B. (2013).
601 Uncovering patterns of near-surface saturated hydraulic conductivity in an overland
602 flow-controlled landscape. *Geoderma*, 195, 1–11.